Structural Engineering and Mechanics, Vol. 35, No. 4 (2010) 511-533
DOI: http://dx.doi.org/10.12989/sem.2010.35.4.511

Meshless equilibrium on line method (MELM) for linear elasticity

A. Sadeghirad*, S. Mohammadi and I. Mahmoudzadeh Kani

School of Civil Engineering, University of Tehran, P.O. Box 11365-4563, Tehran, Iran

(Received July 2, 2007, Accepted February 19, 2010)

Abstract. As a truly meshfree method, meshless equilibrium on line method (MELM), for 2D elasticity problems is presented. In MELM, the problem domain is represented by a set of distributed nodes, and equilibrium is satisfied on lines for any node within this domain. In contrary to conventional meshfree methods, test domains are lines in this method, and all integrals can be easily evaluated over straight lines along x and y directions. Proposed weak formulation has the same concept as the equilibrium on line method which was previously used by the authors for enforcement of the Neumann boundary conditions in the strong-form meshless methods. In this paper, the idea of the equilibrium on line method is developed to use as the weak forms of the governing equations at inner nodes of the problem domain. The moving least squares (MLS) approximation is used to interpolate solution variables in this paper. Numerical studies have shown that this method is simple to implement, while leading to accurate results.

Keywords: computational mechanics; meshfree methods; equilibrium on line method (MELM); moving least squares (MLS) approximation; elasticity.

1. Introduction

Due to the possibility of overcoming the drawbacks of mesh-based methods, such as the difficulty of mesh generation, locking, poor derivative solutions, mesh distortion and the need to remeshing the entire problem domain, meshfree methods have attracted much attention in computational mechanics in recent decade.

Meshfree methods can be classified into two major categories: meshfree methods based on strong forms (or meshfree strong-form methods), such as the general finite difference method (Perrone and Kao 1975), the smoothed particle hydrodynamics (SPH) (Lucy 1977, Gingold and Monaghan 1977), Kansa's method (Kansa 1990), method of fundamental solution (Golberg 1995), hp-meshless cloud method (Liszka *et al.* 1996), the finite point method (FPM) (Onate *et al.* 1996), the least-squares collocation meshless method (Zhang *et al.* 2001), boundary knot method (Chen and Hon 2003), the meshfree point collocation method (MPCM) (Lee and Yoon 2004), radial point interpolation collocation method (Liu *et al.* 2005), least-squares radial point interpolation collocation method (Liu *et al.* 2006a), etc.; and meshfree methods based on weak forms (or meshfree weak-form methods) such as the diffuse element method (DEM) (Nayroles *et al.* 1992), the element-free Galerkin (EFG)

*Corresponding author, Ph.D., E-mail: arsadegh@ut.ac.ir

method (Belytschko *et al.* 1994), the reproducing kernel particle method (RKPM) (Liu *et al.* 1995), point interpolation method (PIM) (Liu and Gu 2001a), radial point interpolation method (RPIM) (Wang *et al.* 2001), linearly conforming radial point interpolation method (LCRPIM) (Liu *et al.* 2006b), mesh-free minimum length method (MLM) (Liu *et al.* 2006c), etc.

Meshfree weak-form methods have been successfully applied to solid mechanics. However, most of meshfree weak-form methods are "meshfree" only in terms of interpolation of the field variables and they have to use background cells to integrate a weak form over the global problem domain; avoiding them of being 'truly' meshfree methods. As a result, a computationally expensive numerical integration is required. In order to alleviate the global integration background mesh, a group of meshfree methods based on the local Petrov-Galerkin weak forms (or meshfree local weak-form methods) have been developed, such as the meshless local Petrov-Galerkin (MLPG) method (Atluri and Zhu 1998), the local boundary integral equation (LBIE) method (Zhu *et al.* 1998), the method of finite spheres (De and Bathe 2000), local point interpolation method (LPIM) (Liu and Gu 2001b), local radial point interpolation method (LRPIM) (Liu and Gu 2001c), etc.

In this paper, a novel 'truly' meshfree method is proposed for 2D elasticity analyses. In contrary to conventional meshfree methods, in this method test domains are straight lines along x and y directions. All integrals can be easily evaluated over these lines. In the MELM, the domain of problem is represented by a set of distributed nodes and equilibrium on lines is satisfied for any node within the domain. The proposed method is a 'truly' meshfree one as it needs no mesh, neither for the purpose of interpolation of the solution variables, nor for the integration of the equilibrium on lines. Proposed weak formulation has the same concept as those previously used by the authors for enforcement of the Neumann boundary conditions in the strong-form meshless methods (Sadeghirad and Mohammadi 2007, Sadeghirad and Mahmoudzadeh Kani 2009). Meshless collocation methods using this idea for imposing the Neumann boundary conditions have been successfully applied for analyzing the elastodynamics and fracture mechanics problems (Sadeghirad *et al.* 2009, Sadeghirad *et al.* 2010). In this work, the idea of the equilibrium on line method is developed to use as the weak forms of the governing equations at inner nodes of the problem domain. The resultant method is a novel weak-form meshless method in which all required integrals are simply calculated over straight lines. One major advantage of the weak-form meshless methods in comparison with the strong-form methods is that they exhibit good stability and accuracy. However, complicated numerical integration makes them computationally expensive (Liu and Gu 2003). Numerical investigations show that proposed weak formulation leads to more accurate and stable results in comparison with those obtained from the direct collocation method.

The MELM uses the moving least squares (MLS) approximation to interpolate the set of solution variables (Lancaster and Salkauskas 1981, Cleveland 1993). The organization of this paper is as follows: a brief description of the MLS approximation is presented in Section 2. Section 3 is dedicated to the MELM formulation and discretization of governing equations. Numerical examples for 2D elasticity problems are given in Section 4, followed by the concluding remarks.

2. The MLS approximation scheme

This section gives a brief summary of the MLS approximation to approximate the components of the displacement field over the problem domain. The MLS interpolant $u^h(\mathbf{x})$ of displacement $u(\mathbf{x})$ is defined in the domain Ω by

$$u(\mathbf{x}) \cong u^h(\mathbf{x}) = \sum_{j=1}^{m} p_j(\mathbf{x}) a_j(\mathbf{x}) = \mathbf{p}^T(\mathbf{x})\mathbf{a}(\mathbf{x}) \tag{1}$$

where $\mathbf{p}(\mathbf{x})$ is a vector of basis monomials and $\mathbf{a}^T(\mathbf{x}) = [a_1(\mathbf{x}), a_2(\mathbf{x}), \ldots, a_m(\mathbf{x})]$ is a vector of coefficients; where m is the number of basis monomials. The coefficients $a_j(\mathbf{x})$ in Eq. (1) are also functions of $\mathbf{x}$; $\mathbf{a}(\mathbf{x})$ is obtained at any point $\mathbf{x}$ by minimizing a weighted, discrete L_2 norm as follows

$$J = \sum_{i=1}^{n} w(\mathbf{x}-\mathbf{x}_i)[\bar{u}_i - u^h(\mathbf{x}_i)]^2 = \sum_{i=1}^{n} w(\mathbf{x}-\mathbf{x}_i)[\bar{u}_i - \mathbf{p}^T(\mathbf{x}_i)\mathbf{a}(\mathbf{x}_i)]^2 \tag{2}$$

where n is the number of nodes in the neighborhood of point $\mathbf{x}$ for which the weight function $w(\mathbf{x}-\mathbf{x}_i) \neq 0$. This neighborhood of $\mathbf{x}$ is called the domain of influence of $\mathbf{x}$. $\bar{u}_i$ is the displacement at $\mathbf{x} = \mathbf{x}_i$, while $u^h(\mathbf{x}_i)$ is the approximate value. Using the stationarity condition for J in Eq. (2) with respect to $\mathbf{a}(\mathbf{x})$ leads to

$$\mathbf{A}(\mathbf{x})\mathbf{a}(\mathbf{x}) = \mathbf{B}(\mathbf{x})\bar{\mathbf{u}} \tag{3}$$

or

$$\mathbf{a}(\mathbf{x}) = \mathbf{A}^{-1}(\mathbf{x})\mathbf{B}(\mathbf{x})\bar{\mathbf{u}} \tag{4}$$

where matrices $\mathbf{A}(\mathbf{x})$ and $\mathbf{B}(\mathbf{x})$ are defined by

$$\mathbf{A}(\mathbf{x}) = \sum_{i=1}^{n} w_i(\mathbf{x})\mathbf{p}(\mathbf{x}_i)\mathbf{p}^T(\mathbf{x}_i), \quad w_i(\mathbf{x}) \equiv w_i(\mathbf{x}-\mathbf{x}_i) \tag{5}$$

$$\mathbf{B}(\mathbf{x}) = [w_1(\mathbf{x})\mathbf{p}(\mathbf{x}_1), w_2(\mathbf{x})\mathbf{p}(\mathbf{x}_2), \ldots, w_n(\mathbf{x})\mathbf{p}(\mathbf{x}_n)] \tag{6}$$

The final approximated displacement is obtained by substituting $\mathbf{a}(\mathbf{x})$ from Eq. (4) into Eq. (1)

$$u^h(\mathbf{x}) = \mathbf{p}^T(\mathbf{x})\mathbf{A}^{-1}(x)\mathbf{B}(x)\bar{\mathbf{u}} = \sum_{i=1}^{n}\sum_{j=1}^{m} p_j(\mathbf{x})(\mathbf{A}^{-1}(\mathbf{x})\mathbf{B}(\mathbf{x}))_{ji}\bar{u}_i \equiv \sum_{i=1}^{n} \phi_i(\mathbf{x})\bar{u}_i \tag{7}$$

where the MLS shape function $\phi_i(x)$ is defined by

$$\phi_i = \sum_{j=1}^{m} p_j(\mathbf{x})(\mathbf{A}^{-1}(\mathbf{x})\mathbf{B}(\mathbf{x}))_{ji} \tag{8}$$

A Gaussian weight function with the compact support property is considered in the present work. The weight function corresponding to node i may be written as

$$w_i(r_i) = \begin{cases} \dfrac{\exp\left[-\left(\dfrac{r_i}{c_i}\right)^{2k}\right] - \exp\left[-\left(\dfrac{r_{m_i}}{c_i}\right)^{2k}\right]}{1 - \exp\left[-\left(\dfrac{r_{m_i}}{c_i}\right)^{2k}\right]}, & 0 \le r_i \le r_{m_i} \\ 0, & r_i > r_{m_i} \end{cases} \tag{9}$$

where $r_i = |\mathbf{x}-\mathbf{x}_i|$ is the distance from node $\mathbf{x}_i$ to point $\mathbf{x}$, c_i is a constant controlling the shape of the weight function w_i and therefore the relative weights. r_{m_i} is the size of the support of the weight

function w_i and determines the domain of influence of $\mathbf{x}$. Note that when c_i decreases, higher weights are obtained on nodes $\mathbf{x}_i$ close to point $\mathbf{x}$ and lower weights on nodes far removed from $\mathbf{x}$. In this paper, c_i is defined as

$$c_i = \alpha \bar{c}_i, \quad \alpha = 1/5 \tag{10}$$

$$\bar{c}_i = \max|\mathbf{x}_j - \mathbf{x}_i|, \quad j \in S_i \tag{11}$$

where S_i is the minimum set of neighboring nodes of $\mathbf{x}_i$ which construct a polygon surrounding node $\mathbf{x}_i$ and α is a user defined parameter. Effects of different values of this parameter on the ELM results have been investigated in (Sadeghirad and Mahmoudzadeh Kani 2009). The performance of this weight function with $k = 1$ will be examined in the numerical examples in section 4.

3. The meshless equilibrium on line method (MELM)

In the MELM, the problem domain is represented by a set of distributed nodes, and governing differential equations are integrated over straight lines along x and y directions. The length of these lines is an important parameter affecting the performance of MELM. In the present work, the length of the lines for a node $\mathbf{x}_i$ is defined as

$$L_i = \beta d_{\min_i} \tag{12}$$

where $d_{\min_i}$ is the distance from node $\mathbf{x}_i$ to the nearest node around it (Fig. 1).

The integrals can be easily evaluated over the lines via Gauss quadrature technique. This integration is computationally efficient, as the integration domains are straight finite lines.

Although the present approach can be generally applied to solving general boundary value problems, only the linear elasticity equations are examined in the following to demonstrate the MELM formulation. The governing equations for linear elasticity problems can be written as

$$\frac{\partial \sigma_{ij}}{\partial x_j} + b_i = 0 \quad \text{in} \quad \Omega \tag{13}$$

where Ω is the global domain bounded by Γ, σ_{ij} is the stress tensor corresponding to the displacement field u_i, b_i is the body force, and $(\,)_{,i}$ denotes $\partial(\,)/\partial x^i$. The corresponding boundary conditions are given as follows

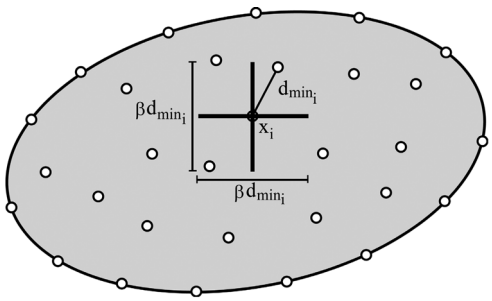

Fig. 1 Determination of the length of the integration lines correspondence to node $\mathbf{x}_i$

$$u_j - \bar{u}_j = 0 \quad \text{on} \quad \Gamma_u \tag{14a}$$

$$\sigma_{ij} n_j - \bar{t}_i = 0 \quad \text{on} \quad \Gamma_t \tag{14b}$$

where $\bar{u}_j$ and $\bar{t}_i$ are the prescribed displacements and tractions over the Dirichlet boundary Γ_u and Neumann boundary Γ_t, respectively, and n_j is the unit outward normal vector to the boundary Γ.

The stress vector is related to the strain vector by the standard Hook's law

$$\boldsymbol{\sigma} = \mathbf{D}\boldsymbol{\varepsilon} \tag{15}$$

where $\mathbf{D}$ is the elastic constitutive matrix and $\boldsymbol{\sigma}$ and $\boldsymbol{\varepsilon}$ are the stress and strain vectors respectively. They are defined in 2D problems as

$$\boldsymbol{\sigma} = [\sigma_{11}, \sigma_{22}, \sigma_{12}]^T \tag{16a}$$

$$\boldsymbol{\varepsilon} = [\varepsilon_{11}, \varepsilon_{22}, \varepsilon_{12}]^T \tag{16b}$$

$$\mathbf{D} = \begin{bmatrix} D_{11} & D_{12} & 0 \\ D_{21} & D_{22} & 0 \\ 0 & 0 & D_{33} \end{bmatrix} \tag{16c}$$

$$D_{11} = D_{22} = \frac{E}{1-\nu^2},\ D_{12} = D_{21} = \frac{\nu E}{1-\nu^2},\ D_{33} = \frac{E}{1+\nu} \text{ for plane stress} \tag{16d}$$

$$D_{11} = D_{22} = \frac{E(1-\nu)}{(1+\nu)(1-2\nu)},\ D_{12} = D_{21} = \frac{E\nu}{(1+\nu)(1-2\nu)},\ D_{33} = \frac{E}{1+\nu} \text{ for plane strain} \tag{16e}$$

Strain components ε_{ij} are related to the displacements by

$$\varepsilon_{ij} = \frac{1}{2}\left(\frac{\partial u_i}{\partial x_j} + \frac{\partial u_j}{\partial x_i}\right) \tag{17}$$

Let Γ_{x_i} and Γ_{y_i} be the straight lines passing through node $\mathbf{x}_i$ which are along x and y directions, respectively (Fig. 2). Each point on these lines is governed by the differential equilibrium Eq. (13). This equation is rewritten in the following form along x and y directions

$$\frac{\partial \sigma_{xx}}{\partial x} + \frac{\partial \sigma_{xy}}{\partial y} + b_x = 0 \tag{18a}$$

$$\frac{\partial \sigma_{xy}}{\partial x} + \frac{\partial \sigma_{yy}}{\partial y} + b_y = 0 \tag{18b}$$

Now Eq. (18) can be integrated over the line Γ_{x_i}

$$[\sigma_{xx}]_P^Q + \int_{\Gamma_{x_i}} \left(\frac{\partial \sigma_{xy}}{\partial y}\right) dx + \int_{\Gamma_{x_i}} b_x dx = 0 \tag{19a}$$

$$[\sigma_{xy}]_P^Q + \int_{\Gamma_{x_i}} \left(\frac{\partial \sigma_{yy}}{\partial y}\right) dx + \int_{\Gamma_{x_i}} b_y dx = 0 \tag{19b}$$

where P and Q are the start and end points of line Γ_{x_i}, respectively (Fig. 2). Eq. (18) can be also integrated over the line Γ_{y_i}

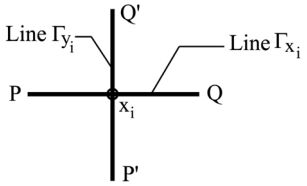

Fig. 2 The Γ_{x_i} and Γ_{y_i} lines and their start and end points

$$\int_{\Gamma_{y_i}} \left(\frac{\partial \sigma_{xx}}{\partial x} \right) dy + [\sigma_{xy}]_{P'}^{Q'} + \int_{\Gamma_{y_i}} b_x dy = 0 \tag{20a}$$

$$\int_{\Gamma_{y_i}} \left(\frac{\partial \sigma_{xy}}{\partial x} \right) dy + [\sigma_{yy}]_{P'}^{Q'} + \int_{\Gamma_{y_i}} b_y dy = 0 \tag{20b}$$

where P' and Q' are the start and end points of line Γ_{y_i}, respectively (Fig. 2). The proposed MELM formulation can now be further extended in two alternatives: (1) balanced line (B-Line) approach and (2) balanced area (B-Area) approach.

3.1 Alternative 1: balanced line (B-Line) approach

In this alternative, Eqs. (19), (20) are directly used for discretization. These equations have the physical meaning of representing the equilibrium law on the so-called B-Lines. Consider B-Lines and their associated applied stresses as depicted in Fig. 3.

The final formulation can be obtained by substituting stress and strain components from Eq. (15)-(17) into Eq. (19), (20) giving

$$\left[D_{11} \frac{\partial u_x}{\partial x} + D_{12} \frac{\partial u_y}{\partial y} \right]_P^Q + \int_{\Gamma_{x_i}} \frac{D_{33}}{2} \left(\frac{\partial^2 u_x}{\partial y^2} + \frac{\partial^2 u_y}{\partial x \partial y} \right) dx + \int_{\Gamma_{x_i}} b_x dx = 0 \tag{21a}$$

$$\left[\frac{D_{33}}{2} \left(\frac{\partial u_x}{\partial y} + \frac{\partial u_y}{\partial x} \right) \right]_P^Q + \int_{\Gamma_{x_i}} \left[D_{21} \frac{\partial^2 u_x}{\partial x \partial y} + D_{22} \frac{\partial^2 u_y}{\partial y^2} \right] dx + \int_{\Gamma_{x_i}} b_y dx = 0 \tag{21b}$$

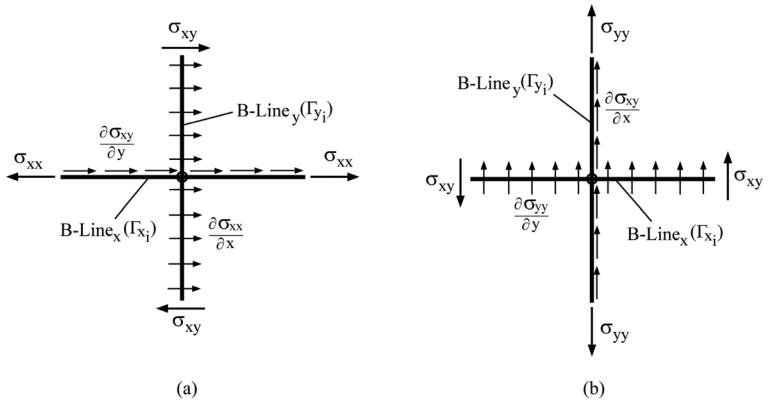

Fig. 3 The B-Lines and stresses applied on them: (a) in x direction and (b) in y direction

$$\int_{\Gamma_{y_i}} \left[D_{11} \frac{\partial^2 u_x}{\partial x^2} + D_{12} \frac{\partial^2 u_y}{\partial x \partial y} \right] dy + \left[\frac{D_{33}}{2} \left(\frac{\partial u_x}{\partial y} + \frac{\partial u_y}{\partial x} \right) \right]_{P'}^{Q'} + \int_{\Gamma_{y_i}} b_x dy = 0 \tag{21c}$$

$$\int_{\Gamma_{y_i}} \frac{D_{33}}{2} \left(\frac{\partial^2 u_x}{\partial x \partial y} + \frac{\partial^2 u_y}{\partial x^2} \right) dy + \left[D_{21} \frac{\partial u_x}{\partial x} + D_{22} \frac{\partial u_y}{\partial y} \right]_{P'}^{Q'} + \int_{\Gamma_{y_i}} b_y dy = 0 \tag{21d}$$

By substituting Eq. (7) into Eq. (21) for all nodes within the problem domain, it leads to the following discretized system of linear algebraic equations

$$\sum_{j=1}^{N} \mathbf{K}_{L_{ij}}^{(p)} \hat{\mathbf{u}}_j = f_{L_i}^{(p)}, \quad p = 1, 2, 3, 4, \; i = 1, 2, \ldots, N \tag{22}$$

where N is the total number of nodes on the problem domain, and $\hat{\mathbf{u}}_j$ is the vector of unknown parameters associated to node j, and

$$\mathbf{K}_{L_{ij}}^{(1)} = \left[D_{11} \left[\frac{\partial \phi_j}{\partial x} \right]_P^Q + \int_{\Gamma_{x_i}} \frac{D_{33}}{2} \frac{\partial^2 \phi_j}{\partial y^2} dx \quad D_{12} \left[\frac{\partial \phi_j}{\partial y} \right]_P^Q + \int_{\Gamma_{x_i}} \frac{D_{33}}{2} \frac{\partial^2 \phi_j}{\partial x \partial y} dx \right] \tag{23a}$$

$$\mathbf{K}_{L_{ij}}^{(2)} = \left[\frac{D_{33}}{2} \left[\frac{\partial \phi_j}{\partial y} \right]_P^Q + \int_{\Gamma_{x_i}} D_{21} \frac{\partial^2 \phi_j}{\partial x \partial y} dx \quad \frac{D_{33}}{2} \left[\frac{\partial \phi_j}{\partial x} \right]_P^Q + \int_{\Gamma_{x_i}} D_{22} \frac{\partial^2 \phi_j}{\partial y^2} dx \right] \tag{23b}$$

$$\mathbf{K}_{L_{ij}}^{(3)} = \left[\frac{D_{33}}{2} \left[\frac{\partial \phi_j}{\partial y} \right]_{P'}^{Q'} + \int_{\Gamma_{y_i}} D_{11} \frac{\partial^2 \phi_j}{\partial x^2} dy \quad \frac{D_{33}}{2} \left[\frac{\partial \phi_j}{\partial x} \right]_{P'}^{Q'} + \int_{\Gamma_{y_i}} D_{12} \frac{\partial^2 \phi_j}{\partial x \partial y} dy \right] \tag{23c}$$

$$\mathbf{K}_{L_{ij}}^{(4)} = \left[D_{21} \left[\frac{\partial \phi_j}{\partial x} \right]_{P'}^{Q'} + \int_{\Gamma_{y_i}} \frac{D_{33}}{2} \frac{\partial^2 \phi_j}{\partial x \partial y} dy \quad D_{22} \left[\frac{\partial \phi_j}{\partial y} \right]_{P'}^{Q'} + \int_{\Gamma_{y_i}} \frac{D_{33}}{2} \frac{\partial^2 \phi_j}{\partial x^2} dy \right] \tag{23d}$$

and

$$f_{L_i}^{(1)} = -\int_{\Gamma_{x_i}} b_x dx, \quad f_{L_i}^{(2)} = -\int_{\Gamma_{x_i}} b_y dx, \quad f_{L_i}^{(3)} = -\int_{\Gamma_{y_i}} b_x dy, \quad f_{L_i}^{(4)} = -\int_{\Gamma_{y_i}} b_y dy \tag{24}$$

In the discretized system of algebraic Eq. (22), the total number of unknowns is $2N$, while the total number of equations is $4N$. For the purpose of solving this system of algebraic equations, the following four types are examined:

Type 1- The equilibrium law on lines Γ_{x_i} and Γ_{y_i} was only satisfied along x and y directions, respectively. As a result, the number of equations and unknowns would remain the same.

Type 2- The equilibrium law on the line Γ_{x_i} was only satisfied along y direction and the equilibrium law on the line Γ_{y_i} was only satisfied along x direction. As a result, the number of equations and unknowns would be the same.

Type 3- The equilibrium law on both lines Γ_{x_i} and Γ_{y_i}, as one set of lines, was simultaneously satisfied along both x and y directions. As a result, similar number of equations and unknowns are obtained.

Type 4- The discretized system of algebraic Eq. (22) can be solved by using the least-squares method.

3.2 Alternative 2: balanced area (B-Area) approach

In this alternative, in order to estimate $\partial\sigma_{xx}/\partial x, \partial\sigma_{xy}/\partial x, \partial\sigma_{xy}/\partial y$ and $\partial\sigma_{yy}/\partial y$ into Eqs. (19), (20), the following simple finite difference approximations are used (Fig. 4)

$$\frac{\partial\sigma_{xx}}{\partial x}=\frac{\sigma_{xx}\Big|_{\Gamma^2_{y_i}}-\sigma_{xx}\Big|_{\Gamma^1_{y_i}}}{\delta_{x_i}},\quad \frac{\partial\sigma_{xy}}{\partial x}=\frac{\sigma_{xy}\Big|_{\Gamma^2_{y_i}}-\sigma_{xy}\Big|_{\Gamma^1_{y_i}}}{\delta_{x_i}},\quad \frac{\partial\sigma_{xy}}{\partial y}=\frac{\sigma_{xy}\Big|_{\Gamma^2_{x_i}}-\sigma_{xy}\Big|_{\Gamma^1_{x_i}}}{\delta_{y_i}},\quad \frac{\partial\sigma_{yy}}{\partial y}=\frac{\sigma_{yy}\Big|_{\Gamma^2_{x_i}}-\sigma_{yy}\Big|_{\Gamma^1_{x_i}}}{\delta_{y_i}} \tag{25}$$

Substituting Eq. (25) into Eqs. (19), (20) leads to

$$\left[\sigma_{xx}\right]_P^Q+\int_{\Gamma^2_{x_i}}\left(\frac{\sigma_{xy}}{\delta_{y_i}}\right)dx-\int_{\Gamma^1_{x_i}}\left(\frac{\sigma_{xy}}{\delta_{y_i}}\right)dx+\int_{\Gamma_{x_i}}b_x dx=0 \tag{26a}$$

$$\left[\sigma_{xy}\right]_P^Q+\int_{\Gamma^2_{x_i}}\left(\frac{\sigma_{yy}}{\delta_{y_i}}\right)dx-\int_{\Gamma^1_{x_i}}\left(\frac{\sigma_{yy}}{\delta_{y_i}}\right)dx+\int_{\Gamma_{x_i}}b_y dx=0 \tag{26b}$$

$$\int_{\Gamma^2_{y_i}}\left(\frac{\sigma_{xx}}{\delta_{x_i}}\right)dy-\int_{\Gamma^1_{y_i}}\left(\frac{\sigma_{xx}}{\delta_{x_i}}\right)dy+\left[\sigma_{xy}\right]_{P'}^{Q'}+\int_{\Gamma_{y_i}}b_x dy=0 \tag{26c}$$

$$\int_{\Gamma^2_{y_i}}\left(\frac{\sigma_{xy}}{\delta_{x_i}}\right)dy-\int_{\Gamma^1_{y_i}}\left(\frac{\sigma_{xy}}{\delta_{x_i}}\right)dy+\left[\sigma_{yy}\right]_{P'}^{Q'}+\int_{\Gamma_{y_i}}b_y dy=0 \tag{26d}$$

Eq. (26) has the physical meaning of representing the equilibrium law of the B-Area (Fig. 4). The final formulation is obtained by substituting stress and strain components from Eqs. (15)-(17) into Eq. (26) which gives

$$\left[D_{11}\frac{\partial u_x}{\partial x}+D_{12}\frac{\partial u_y}{\partial y}\right]_P^Q+\frac{1}{\delta_{y_i}}\int_{\Gamma^2_{x_i}}\frac{D_{33}}{2}\left(\frac{\partial u_x}{\partial y}+\frac{\partial u_y}{\partial x}\right)dx-\frac{1}{\delta_{y_i}}\int_{\Gamma^1_{x_i}}\frac{D_{33}}{2}\left(\frac{\partial u_x}{\partial y}+\frac{\partial u_y}{\partial x}\right)dx+\int_{\Gamma_{x_i}}b_x dx=0 \tag{27a}$$

$$\left[\frac{D_{33}}{2}\left(\frac{\partial u_x}{\partial y}+\frac{\partial u_y}{\partial x}\right)\right]_P^Q+\frac{1}{\delta_{y_i}}\int_{\Gamma^2_{x_i}}\left[D_{21}\frac{\partial u_x}{\partial x}+D_{22}\frac{\partial u_y}{\partial y}\right]dx-\frac{1}{\delta_{y_i}}\int_{\Gamma^1_{x_i}}\left[D_{21}\frac{\partial u_x}{\partial x}+D_{22}\frac{\partial u_y}{\partial y}\right]dx+\int_{\Gamma_{x_i}}b_y dx=0 \tag{27b}$$

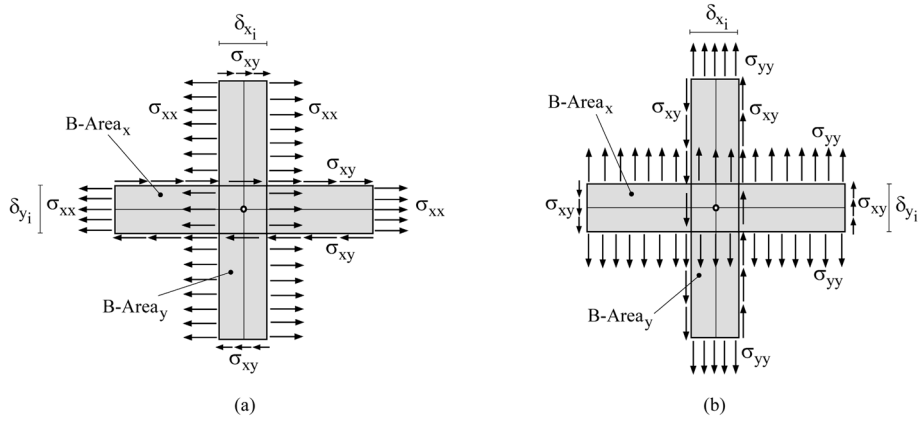

Fig. 4 The B-Areas and stresses applied on them: (a) in x direction, and (b) in y direction

$$\frac{1}{\delta_{x_i}}\int_{\Gamma^2_{y_i}}\left[D_{11}\frac{\partial u_x}{\partial x}+D_{12}\frac{\partial u_y}{\partial y}\right]dy-\frac{1}{\delta_{x_i}}\int_{\Gamma^1_{y_i}}\left[D_{11}\frac{\partial u_x}{\partial x}+D_{12}\frac{\partial u_y}{\partial y}\right]dy+\left[\frac{D_{33}}{2}\left(\frac{\partial u_x}{\partial y}+\frac{\partial u_y}{\partial x}\right)\right]_{P'}^{Q'}+\int_{\Gamma_{y_i}}b_x dy=0 \tag{27c}$$

$$\frac{1}{\delta_{x_i}}\int_{\Gamma^2_{y_i}}\frac{D_{33}}{2}\left(\frac{\partial u_x}{\partial y}+\frac{\partial u_y}{\partial x}\right)dy-\frac{1}{\delta_{x_i}}\int_{\Gamma^1_{y_i}}\frac{D_{33}}{2}\left(\frac{\partial u_x}{\partial y}+\frac{\partial u_y}{\partial x}\right)dy+\left[D_{21}\frac{\partial u_x}{\partial x}+D_{22}\frac{\partial u_y}{\partial y}\right]_{P'}^{Q'}+\int_{\Gamma_{y_i}}b_y dy=0 \tag{27d}$$

By comparison between Eq. (21) and (27) one can see that in contrary to the alternative 1, there are no 2nd order derivatives of displacements in alternative 2.

Substitution of Eq. (7) into Eq. (27) for all nodes leads to the following discretized system of linear algebraic equations

$$\sum_{j=1}^{N}\mathbf{K}^{(p)}_{A_{ij}}\hat{\mathbf{u}}_j=f^{(p)}_{A_i},\quad p=1,2,3,4,\ i=1,2,\ldots,N \tag{28}$$

where

$$\mathbf{K}^{(1)}_{A_{ij}}=\left[D_{11}\left[\frac{\partial\varphi_j}{\partial x}\right]_P^Q+\frac{1}{\delta_{y_i}}\int_{\Gamma^2_{x_i}}\frac{D_{33}}{2}\frac{\partial\varphi_j}{\partial y}\,dx-\frac{1}{\delta_{y_i}}\int_{\Gamma^1_{x_i}}\frac{D_{33}}{2}\frac{\partial\varphi_j}{\partial y}\,dx\quad D_{12}\left[\frac{\partial\varphi_j}{\partial y}\right]_P^Q+\frac{1}{\delta_{y_i}}\int_{\Gamma^2_{x_i}}\frac{D_{33}}{2}\frac{\partial\varphi_j}{\partial x}\,dx-\frac{1}{\delta_{y_i}}\int_{\Gamma^1_{x_i}}\frac{D_{33}}{2}\frac{\partial\varphi_j}{\partial x}\,dx\right] \tag{29a}$$

$$\mathbf{K}^{(2)}_{A_{ij}}=\left[\frac{D_{33}}{2}\left[\frac{\partial\phi_j}{\partial y}\right]_P^Q+\frac{1}{\delta_{y_i}}\int_{\Gamma^2_{x_i}}D_{21}\frac{\partial\phi_j}{\partial x}\,dx-\frac{1}{\delta_{y_i}}\int_{\Gamma^1_{x_i}}D_{21}\frac{\partial\phi_j}{\partial x}\,dx\quad\frac{D_{33}}{2}\left[\frac{\partial\phi_j}{\partial x}\right]_P^Q+\frac{1}{\delta_{y_i}}\int_{\Gamma^2_{x_i}}D_{22}\frac{\partial\phi_j}{\partial y}\,dx-\frac{1}{\delta_{y_i}}\int_{\Gamma^1_{x_i}}D_{22}\frac{\partial\phi_j}{\partial y}\,dx\right] \tag{29b}$$

$$\mathbf{K}^{(3)}_{A_{ij}}=\left[\frac{D_{33}}{2}\left[\frac{\partial\phi_j}{\partial y}\right]_{P'}^{Q'}+\frac{1}{\delta_{x_i}}\int_{\Gamma^2_{y_i}}D_{11}\frac{\partial\phi_j}{\partial x}\,dy-\frac{1}{\delta_{x_i}}\int_{\Gamma^1_{y_i}}D_{11}\frac{\partial\phi_j}{\partial x}\,dy\quad\frac{D_{33}}{2}\left[\frac{\partial\phi_j}{\partial x}\right]_{P'}^{Q'}+\frac{1}{\delta_{x_i}}\int_{\Gamma^2_{y_i}}D_{12}\frac{\partial\phi_j}{\partial y}\,dy-\frac{1}{\delta_{x_i}}\int_{\Gamma^1_{y_i}}D_{12}\frac{\partial\phi_j}{\partial y}\,dy\right] \tag{29c}$$

$$\mathbf{K}^{(4)}_{A_{ij}}=\left[D_{21}\left[\frac{\partial\phi_j}{\partial x}\right]_{P'}^{Q'}+\frac{1}{\delta_{x_i}}\int_{\Gamma^2_{y_i}}\frac{D_{33}}{2}\frac{\partial\phi_j}{\partial y}\,dy-\frac{1}{\delta_{x_i}}\int_{\Gamma^1_{y_i}}\frac{D_{33}}{2}\frac{\partial\phi_j}{\partial y}\,dy\quad D_{22}\left[\frac{\partial\phi_j}{\partial y}\right]_{P'}^{Q'}+\frac{1}{\delta_{x_i}}\int_{\Gamma^2_{y_i}}\frac{D_{33}}{2}\frac{\partial\phi_j}{\partial x}\,dy-\frac{1}{\delta_{x_i}}\int_{\Gamma^1_{y_i}}\frac{D_{33}}{2}\frac{\partial\phi_j}{\partial x}\,dy\right] \tag{29d}$$

and

$$f^{(1)}_{A_i}=-\int_{\Gamma_{x_i}}b_x dx,\quad f^{(2)}_{A_i}=-\int_{\Gamma_{x_i}}b_y dx,\quad f^{(3)}_{A_i}=-\int_{\Gamma_{y_i}}b_x dy,\quad f^{(4)}_{A_i}=-\int_{\Gamma_{y_i}}b_y dy \tag{30}$$

In the discretized system of algebraic Eq. (28), the total number of unknowns is $2N$, while the total number of equations is $4N$. For solving this system of algebraic equations, four different types, similar to the alternative 1, are examined.

In the present study, the standard collocation method is used to impose both the Dirichlet and Neumann boundary conditions, because the MLS shape functions do not satisfy the Kronecker delta condition.

3.3 The MELM flowchart

The implementation of the MELM can be carried out according to the following routine:

1. Choose a finite number of nodes in the domain Ω and on the boundary Γ of the given physical domain; decide the basis functions, weight functions and support domains sizes so that the MLS approximation is well defined; choose between two alternatives available in the MELM: B-Line and B-Area approaches; choose between four types available for both B-Line and B-Area approaches;
2. Loop over nodes located inside the global domain:
   - Determine the integration lines as the test domains corresponding to the considered node $\mathbf{x}_i$

i.e., lines Γ_{x_i} and Γ_{y_i} for the B-Line approach or lines $\Gamma_{x_i}^1$, $\Gamma_{x_i}^2$, $\Gamma_{y_i}^1$ and $\Gamma_{y_i}^2$ for the B-Area approach;

- Loop over the integration lines:
  - Loop over the Gauss points along considered integration line:
  - Determine the nodes $\mathbf{x}_j$ located in the support domain of the MLS approximation for calculating the shape functions at considered Gauss point;
  - Calculate the shape functions and their derivatives at considered Gauss point;
  - Evaluate numerical integrals in Eqs. (23), (24) for the B-Line approach and Eqs. (29), (30) for the B-Area approach;
  - End loop
- Calculate the shape functions at the start and end points of considered integration line;
- Assemble contributions to the global matrices $\mathbf{K}^p$ and $\mathbf{f}^p$ in which $p = 1, 2, 3, 4$ according to Eqs. (22)-(24) for the B-Line approach and (28)-(30) for the B-Area approach;
- End loop

End loop.

3. Form the final stiffness and force matrices $\mathbf{K}$ and $\mathbf{f}$ from global matrices $\mathbf{K}^p$ and $\mathbf{f}^p$ according to the chosen type in step 1:

- Type 1: $\begin{cases} \mathbf{K}_{2i-1} = \mathbf{K}_i^1 \\ \mathbf{K}_{2i} = \mathbf{K}_i^4 \end{cases}, \quad i = 1, \ldots, N$
- Type 2: $\begin{cases} \mathbf{K}_{2i-1} = \mathbf{K}_i^3 \\ \mathbf{K}_{2i} = \mathbf{K}_i^2 \end{cases}, \quad i = 1, \ldots, N$
- Type 3: $\begin{cases} \mathbf{K}_{2i-1} = \mathbf{K}_i^1 + \mathbf{K}_i^3 \\ \mathbf{K}_{2i} = \mathbf{K}_i^2 + \mathbf{K}_i^4 \end{cases}, \quad i = 1, \ldots, N$
- Type 4: $\begin{cases} \mathbf{K}_{4i-3} = \mathbf{K}_i^1 \\ \mathbf{K}_{4i-2} = \mathbf{K}_i^2 \\ \mathbf{K}_{4i-1} = \mathbf{K}_i^3 \\ \mathbf{K}_{4i} = \mathbf{K}_i^4 \end{cases}, \quad i = 1, \ldots, N$

(Type 4 leads to an overdetermined system of algebraic equations which should be solved with the least-squares method in step 5.)

4. Loop over nodes located at the Dirichlet boundary Γ_u or at the Neumann boundary Γ_t:
   - Determine the nodes $\mathbf{x}_j$ located in the support domain of the MLS approximation for calculating the shape functions at considered boundary node;
   - Calculate the shape functions and their derivatives at considered boundary node;
   - Calculate contributions of the boundary condition equations by directly imposing conditions (14a) and (14b) to the approximated displacements and stresses obtained from the MLS approximation at the boundary node;
   - Assemble contributions to the linear system $\mathbf{K}$ and $\mathbf{f}$;

   (Detailed discussion of the formulation to directly enforce the Dirichlet and Neumann boundary conditions is presented in Appendix A).

End loop.

5. Solve the linear system for the nominal nodal values $\hat{\mathbf{u}}$.
6 Calculate the displacements and their derivatives by using Eqs. (7), (8) at those sample points under consideration.

4. Numerical examples

Several numerical examples of two-dimensional elastostatics are studied to illustrate the performance of the proposed method. A quadratic displacement interpolation ($m = 6$) is chosen for the analysis. Unless stated otherwise, in application of the MELM, the length of lines for each node is defined as $L_i = 2d_{\min_i}$, where $d_{\min_i}$ is the distance from node $\mathbf{x}_i$ to its nearest node, and the width of B-Area is chosen as $\delta = L_s/5$, where L_s is the length of B-Area, and Type 3 of B-Line and B-Area approaches is applied. Also, the size of the support domains (r_{m_i}) is defined as $r_{m_i} = 2.5\bar{c}_i$, where $\bar{c}_i$ is defined in Eq. (11). Numerical integration is carried out using only 3 quadrature points for each line. The mechanical parameters are taken as $E = 1000$ and $\nu = 0.25$ in all numerical investigations. Also, first three examples are solved for plane stress case and in the last one plane strain case is assumed.

For the purpose of error estimation and convergence studies, the following error norm is adopted (Boroomand *et al.* 2005, Sadeghirad and Mohammadi 2007).

$$Error = \begin{cases} \sqrt{\frac{1}{N}\sum_{i=1}^{N}[(u_x^{exact})_i - (u_x^{num})_i]^2}, & \text{for displacement } u_x \\ \sqrt{\frac{1}{N}\sum_{i=1}^{N}[(u_y^{exact})_i - (u_y^{num})_i]^2}, & \text{for displacement } u_y \\ \sqrt{\frac{1}{N}\sum_{i=1}^{N}[(\sigma_{xx}^{exact})_i - (\sigma_{xx}^{num})_i]^2}, & \text{for stress } \sigma_{xx} \\ \sqrt{\frac{1}{N}\sum_{i=1}^{N}[(\sigma_{xy}^{exact})_i - (\sigma_{xy}^{num})_i]^2}, & \text{for stress } \sigma_{xy} \end{cases} \tag{31}$$

In which $(u_x^{exact})_i, (u_y^{exact})_i, (\sigma_{xx}^{exact})_i$ and $(\sigma_{xy}^{exact})_i$ are the exact values of u_x, u_y, σ_{xx} and σ_{xy} at node i respectively; $(u_x^{num})_i, (u_y^{num})_i, (\sigma_{xx}^{num})_i$ and $(\sigma_{xy}^{num})_i$ are the results at node i obtained from the numerical simulation; and N is the total number of nodes.

4.1 Patch test

A high-order patch test with second-order displacement field is studied. A linearly varying axial stress is applied on the right end of the patch while other boundaries of the patch are Dirichlet boundaries as shown in Fig. 5. The exact solution for this problem is assumed as

$$u_i = x_i y_i - y_i + 2, \quad v_i = -(4x_i^2 + y_i^2)/8 + x_i + 1 \tag{32}$$

The analytical values for the displacements and stresses are obtained by using both alternatives of

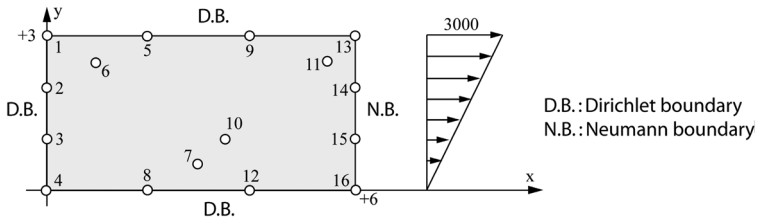

Fig. 5 A higher-order patch test with 16 irregular nodes

Table 1 Numerical results for a patch test with 16 irregular nodes*

Nodes	Coordinates	u_i	v_i	$(\sigma_{xx})_i$	$(\sigma_{yy})_i$	$(\sigma_{xy})_i$
6	(1,2.5)	2.000000	0.718750	2500.000000	0.000000	0.000000
7	(3,0.5)	3.000000	−0.531250	500.000000	0.000000	0.000000
10	(3.5,1)	4.500000	−1.750000	1000.000000	0.000000	0.000000
11	(5.5,2.5)	13.250000	−9.406250	2500.000000	0.000000	0.000000

*All numerical results coincide with the analytical values by six digits.

the MELM (see Table 1). The used MLS shape functions can reproduce second-order polynomials and the boundary conditions are exactly enforced. Therefore, the MELM has the capability of exactly reproducing the displacement and stress fields of the patch test if the required numerical integrations in the MELM are exactly calculated. However, the MLS shape functions have no simple polynomial form and the integration cannot be exactly evaluated and some errors appear in the numerical results. These errors are small because the required integrals over straight lines in the MELM can be evaluated with appropriate accuracy by the Gauss quadrature technique. The observed errors of the calculated displacements and stresses in this example are less than 10^{-7}.

4.2 Cantilever beam

Performance of the MELM is studied for a cantilever beam problem (Fig. 6), for which the following exact solution is available (Timoshenko and Goodier 1970)

$$u = \frac{Py}{6EI}\left[(6L-3x)x + (2+\nu)y^2 - \frac{3D^2}{2}(1+\nu)\right] \tag{33a}$$

$$v = \frac{-P}{6EI}[3\nu y^2(L-x)x + (3L-x)x^2] \tag{33b}$$

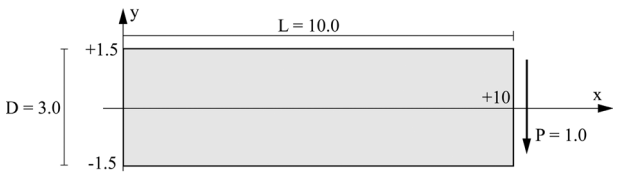

Fig. 6 Geometry of the cantilever beam

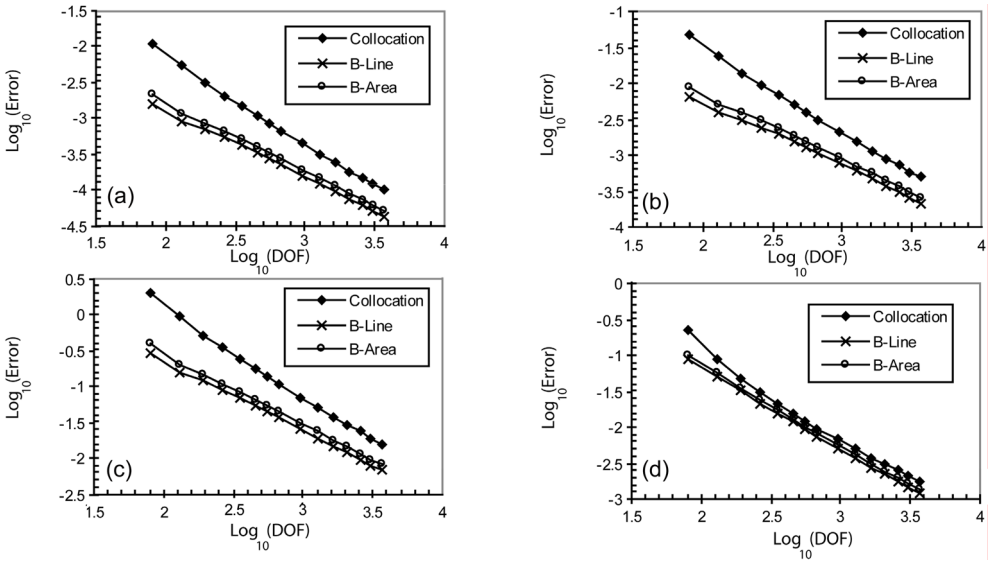

Fig. 7 Rate of convergence for the cantilever beam problem with regular nodal distributions: (a) displacement u_x, (b) displacement u_y, (c) stress σ_{xx}, and (d) stress σ_{xy}

while the stresses are

$$\sigma_{11} = \frac{12P(L-x)y}{D^3}, \quad \sigma_{22} = 0, \quad \sigma_{12} = \frac{-6P}{D^3}\left(\frac{D^2}{4} - y^2\right) \tag{34}$$

In the numerical model, the analytical displacement solution from Eq. (33) is prescribed on the boundary Γ_u: $x = 0$, $-D/2 \le y \le D/2$ (Fig. 7). On the remaining boundaries, exact tractions are specified.

Convergence studies are carried out using fifteen different regular nodal distributions, namely $(10\times4),(13\times5),(16\times6),(19\times7),(22\times8),(25\times9),(28\times10),(31\times11),(37\times13),(43\times15),(49\times17)$, $(55\times19),(61\times21),(67\times23)$ and (73×25) nodes. The convergence curves are presentsd in Fig. 7. For comparison, the convergence curves for the standard collocation method which is discussed in Appendix A, and the MELM are plotted in the same figure (Fig. 7). By application of the MELM an improvement in error values for both displacements and stresses is observed, in comparison to the standard collocation method. Also, values of error in B-Area and B-Line approaches are approximately the same.

The vertical displacement along the neutral axis of the beam and the distribution of shear stress on a cross-section at the mid-span of the beam are depicted in Fig. 8.

Fig. 9 depicts the effects of various MELM types (stated in section 3) in application of B-Line and B-Area approaches. The results clearly show that stable convergence rates are obtained for all types of B-Line and B-Area approaches.

One of the most effective parameters in the MELM method is the length of B-Line or B-Area. So the influence of this parameter is investigated only for a nodal distribution of $225(25\times9)$ nodes. Fig. 10 depicts the error norms of displacements and stresses for different values of $r_1 = L_i/d_{\min_i}$, where L_i is the length of B-Line or B-Area and $d_{\min_i}$ is the distance from node $\mathbf{x}_i$ to the nearest node to it. According to this figure, by increasing the value of r_1, the error is decreased until an

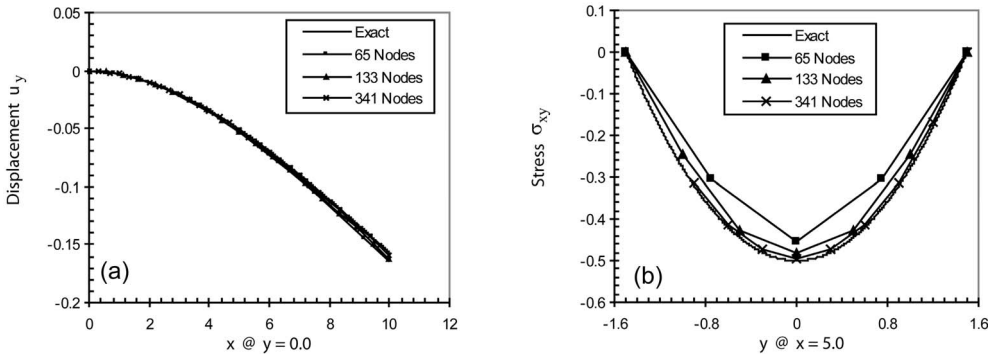

Fig. 8 Cantilever beam analyzed by B-Line approach: (a) distribution of vertical displacement along the neutral axis fiber of the beam, and (b) distribution of shear stress along the central cross-section of the beam

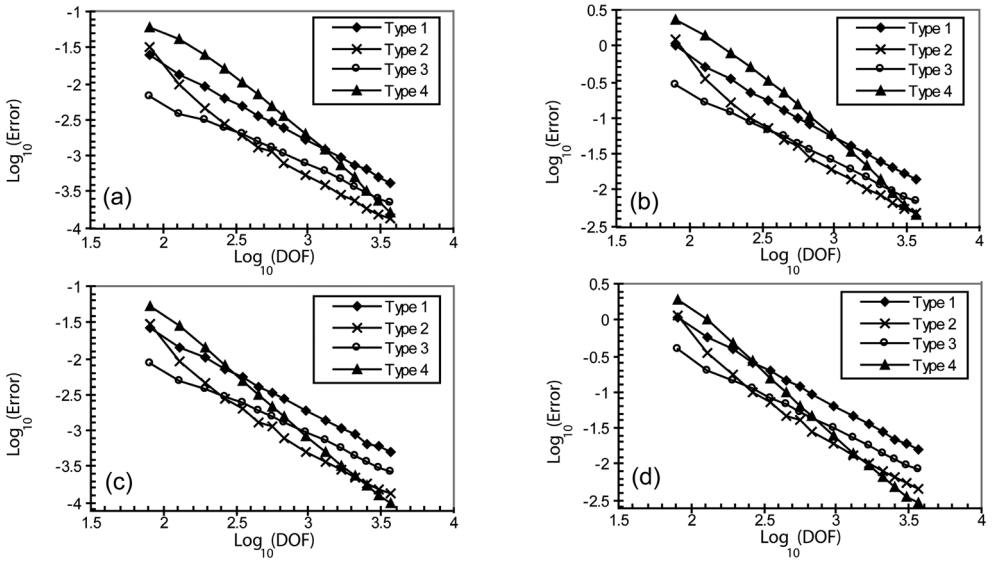

Fig. 9 The error norms of (a,c) displacement u_y and (b,d) stress σ_{xx} in the cantilever beam problem for various types of (a,b) B-Line approach and (c,d) B-Area approach

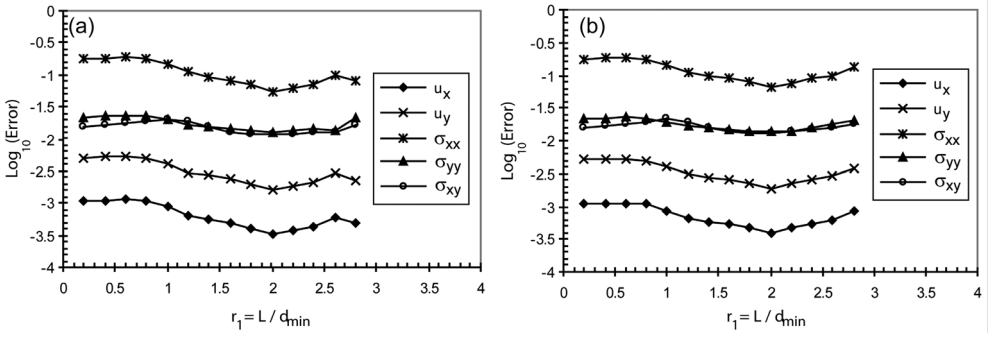

Fig. 10 The error norms of displacements and stresses in the cantilever beam problem for different values of $r_1 = L_i/d_{\min_i}$ for (a) B-Line approach and (b) B-Area approach

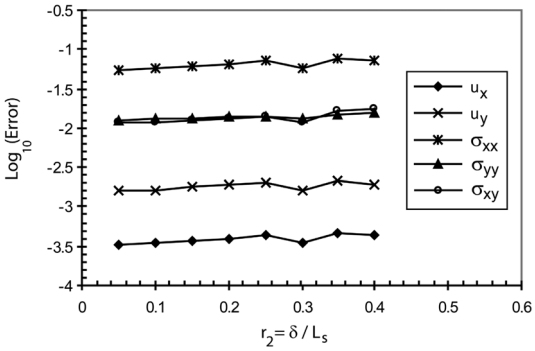

Fig. 11 The error norms of displacements and stresses in the cantilever beam problem for different values of $r_2 = \delta/L_s$ for B-Area approach

optimum value for which the lowest norm of error can be achieved. By further increase in r_1, the error is also increased.

Another effective parameter in the B-Area approach is the width of B-Area. So the influence of this parameter is studied for a nodal distribution of $225(25 \times 9)$ nodes. Fig. 11 depicts the error norms of displacements and stresses for different values of $r_2 = \delta/L_s$, where δ, L_s are the width and length of B-Area, respectively. The results show that the B-Area approach is less sensitive to the width of B-Area for studied range of r_2 values.

4.3 Infinite plate with a circular hole

An infinite plate with a central hole of radius a is considered (Fig. 12). The plate is subjected to a uniform tension, $\bar{t}_x$, in the x direction at infinity. The exact solution for stresses is as follows (Timoshenko and Goodier 1970)

$$\sigma_{11} = \bar{t}_x \left\{ 1 - \frac{a^2}{r^2}\left[\frac{3}{2}\cos(2\theta) + \cos(4\theta)\right] + \frac{3a^4}{2r^4}\cos(4\theta) \right\} \tag{35a}$$

$$\sigma_{22} = -\bar{t}_x \left\{ \frac{a^2}{r^2}\left[\frac{1}{2}\cos(2\theta) - \cos(4\theta)\right] + \frac{3a^4}{2r^4}\cos(4\theta) \right\} \tag{35b}$$

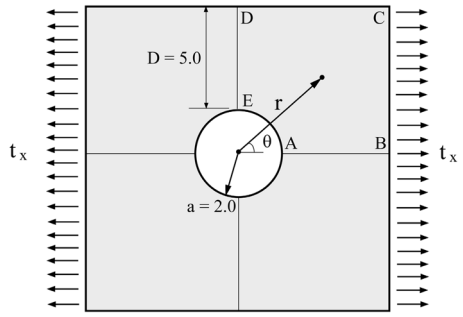

Fig. 12 Infinite plate with a circular hole under tension

$$\sigma_{12} = -\bar{t}_x \left\{ \frac{a^2}{r^2}\left[\frac{1}{2}\sin(2\theta) + \sin(4\theta)\right] - \frac{3a^4}{2r^4}\sin(4\theta) \right\} \tag{35c}$$

The displacement components (rigid-body displacement and rotation set to zero) are

$$u_r = \frac{\bar{t}_x}{4G}\left\{ r\left[\frac{\kappa-1}{2} + \cos(2\theta)\right] + \frac{a^2}{r}[1 + (1+\kappa)\cos(2\theta)] - \frac{a^4}{r^3}\cos(2\theta) \right\} \tag{36a}$$

$$u_\theta = \frac{\bar{t}_x}{4G}\left[(1-\kappa)\frac{a^2}{r} - r - \frac{a^4}{r^3} \right]\sin(2\theta) \tag{36b}$$

where

$$G = \frac{E}{2(1+\nu)}, \quad \kappa = \frac{3-\nu}{1+\nu} \tag{37}$$

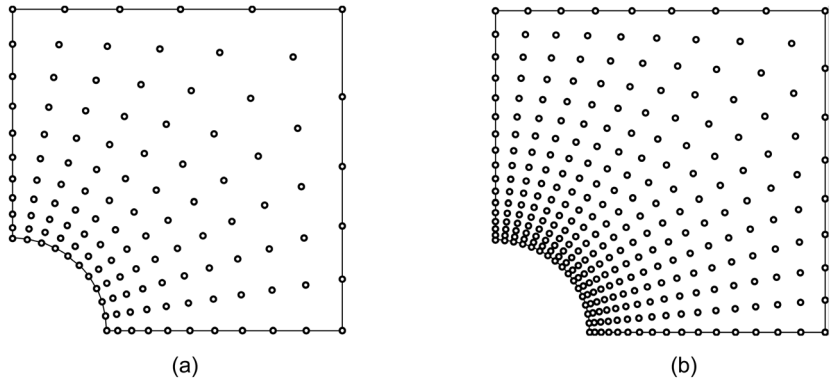

Fig. 13 Sample nodal distributions for modeling the plate with circular hole: (a) 121 nodes, and (b) 289 nodes

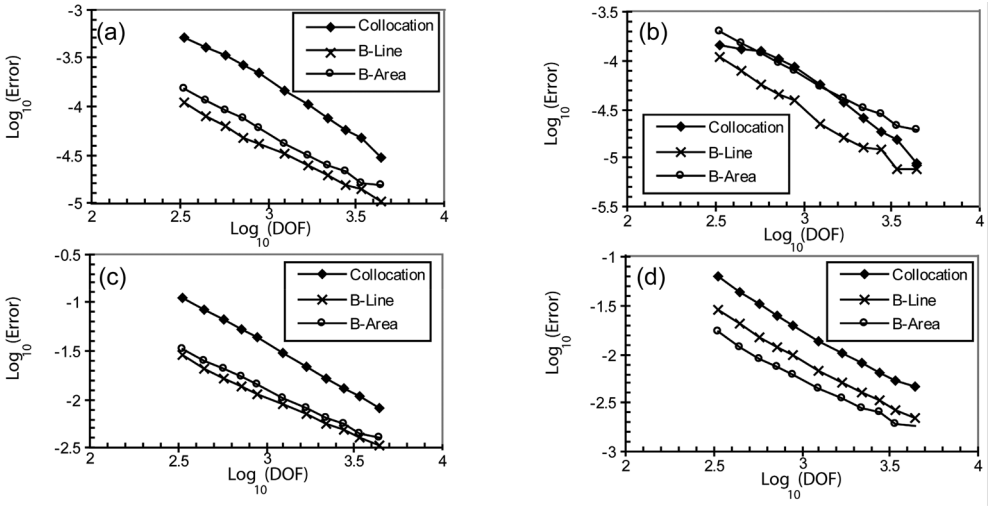

Fig. 14 Rate of convergence for the plate with circular hole with regular nodal distributions: (a) displacement u_x, (b) displacement u_y, (c) stress σ_{xx}, and (d) stress σ_{xy}

Due to symmetry, only one-quarter of the plate is considered. The domain ABCDE shown in Fig. 12 is modeled with the exact tractions imposed along BC and CD. Due to symmetry, the essential boundary conditions are: $u_2 = 0$ along AB, and $u_1 = 0$ along DE.

Convergence studies are carried out using eleven different nodal distributions, with 169, 225, 289, 361, 441, 625, 841, 1089, 1369, 1681 and 2209 nodes. Fig. 13 illustrates two samples 121-node and 289-node models.

The convergence rates are studied in Fig. 14. The results show that the error values in B-Line and B-Area are less than the error values in the standard collocation method.

Fig. 15 depicts the vertical displacement and the distribution of stress σ_{xx} along the line $x = 0$. The displacement and stress profiles match the analytical solution very well.

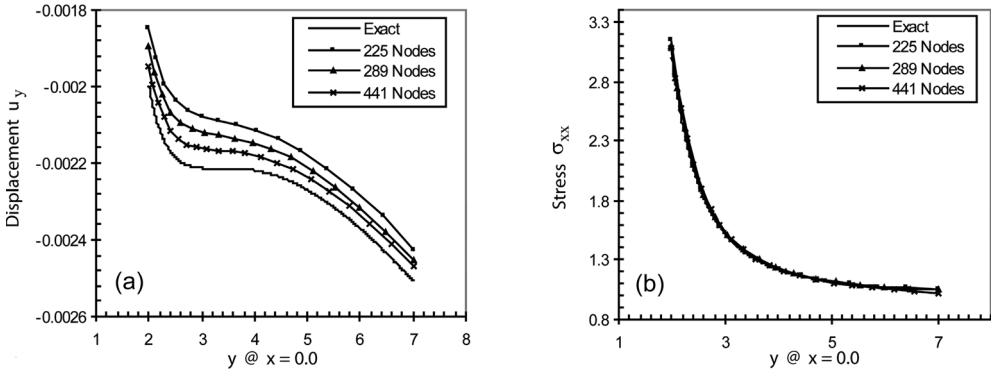

Fig. 15 The plate with circular hole analyzed by B-Line approach: distribution of (a) vertical displacement and (b) stress σ_{xx} along the line $x = 0$

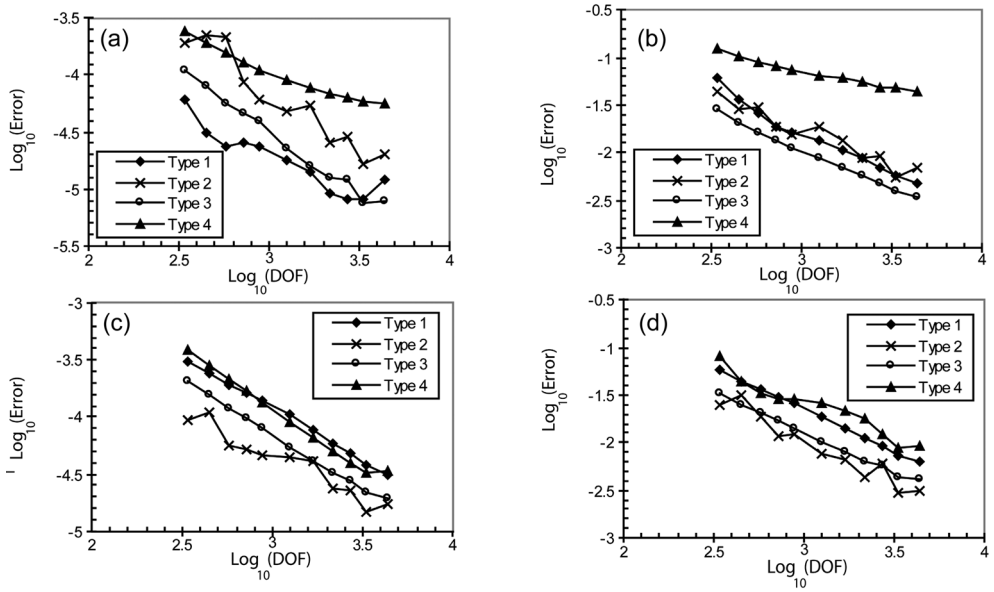

Fig. 16 The error norms of (a,c) displacement u_y and (b,d) stress σ_{xx} in the plate with circular hole for various types of (a,b) B-Line approach, (c,d) B-Area approach

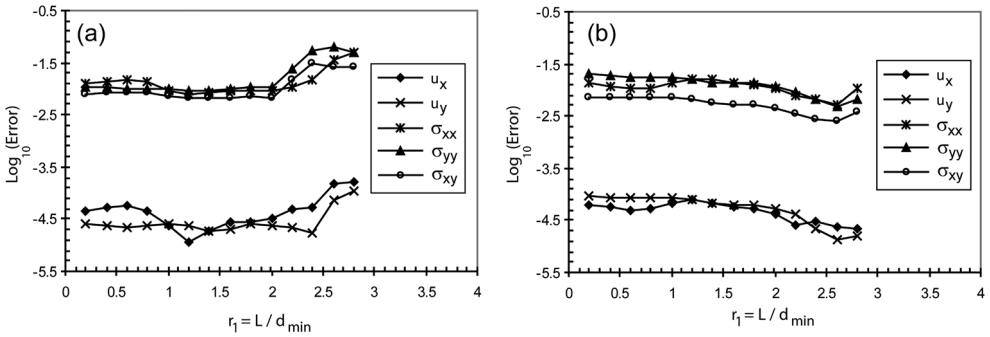

Fig. 17 The error norms of displacements and stresses in the plate with circular hole for different values of $r_1 = L_i/d_{\min_i}$ for (a) B-Line approach; (b) B-Area approach

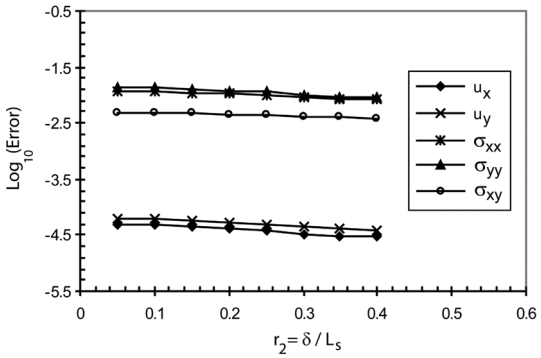

Fig. 18 The error norms of displacements and stresses in the plate with circular hole for different values of $r_2 = \delta/L_s$ for B-Area approach

Effects of various MELM types (stated in section 3) in application of B-Line and B-Area approaches are depicted in Fig. 16.

The influence of the length of B-Line or B-Area is studied for a nodal distribution of 625 nodes. Fig. 17 depicts the error norms of displacements and stresses for different values of $r_1 = L_i/d_{\min_i}$, where L_i is the length of B-Line or B-Area and is $d_{\min_i}$ the distance from node $\mathbf{x}_i$ to the nearest node to it.

The influence of the width of B-Area in the B-Area approach is studied for a nodal distribution of 625 nodes. Fig. 18 depicts the error norms of displacements and stresses for different values of $r_2 = \delta/L_s$, where δ, L_s are the width and length of B-Area, respectively.

4.4 square patch with near-tip field

A cracked square patch with an edge crack is considered here (Fig. 19). Closed-form solutions of mode I crack for plane strain case are (Anderson 1991)

$$u_r = K_I \frac{1+\nu}{E}\sqrt{\frac{r}{2\pi}}\left[\left(\frac{5}{2}-\frac{4\nu}{1+\nu}\right)\cos\frac{\theta}{2}-\frac{1}{2}\cos\frac{3\theta}{2}\right] \tag{38a}$$

$$u_\theta = K_I \frac{1+\nu}{E}\sqrt{\frac{r}{2\pi}}\left[-\left(\frac{7}{2}-\frac{4\nu}{1+\nu}\right)\sin\frac{\theta}{2}+\frac{1}{2}\sin\frac{3\theta}{2}\right] \tag{38b}$$

where r is the distance from the crack tip, θ is the angle from the tangent to the crack path at the crack tip (Fig. 19(a)). Due to the symmetry about the y-axis, only upper half of the patch is modeled. As shown in Fig. 19(b), the known near-tip displacement fields and symmetry boundary conditions are prescribed on the right boundary and segment AB of the lower boundary respectively, while the analytical tractions obtained from the known near-tip displacement fields are specified along other boundaries of the patch. Also, the faces of the crack have the traction-free

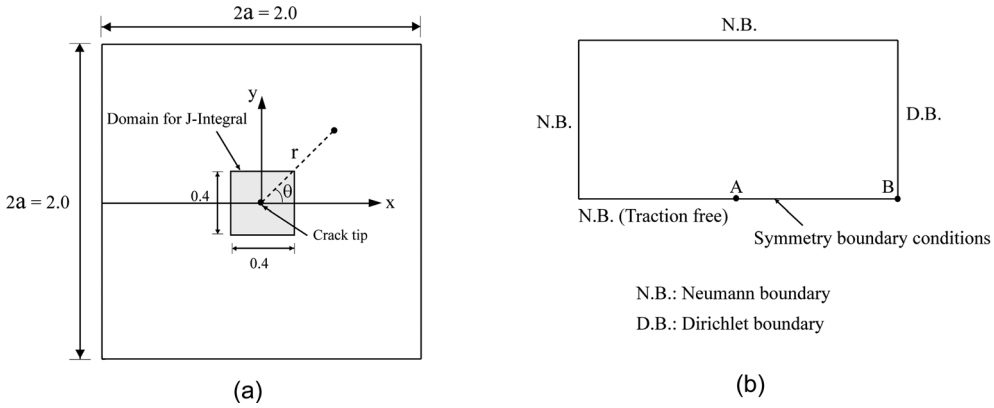

Fig. 19 (a) A square patch with an edge crack, (b) the upper half of patch considered in the computation

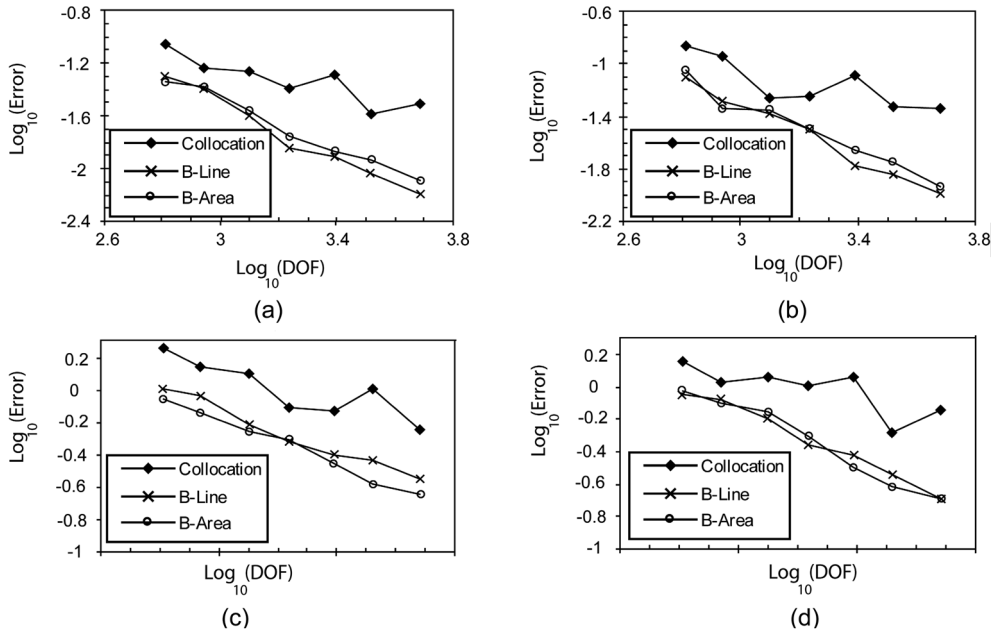

Fig. 20 Rate of convergence for the patch with an edge crack problem with regular nodal distributions: (a) displacement u_x, (b) displacement u_y, (c) stress σ_{xx}, and (d) stress σ_{xy}

Table 2 Comparison of computed stress intensity factors between collocation method and various types of B-Line method

Nodes	Collocation (Error %)	B-Line (Error %) Type 1	B-Line (Error %) Type 2	B-Line (Error %) Type 3	B-Line (Error %) Type 4
13×25	1.0842 (8.42)	1.0498 (4.98)	1.0531 (5.31)	1.0514 (5.14)	1.0702 (7.02)
15×29	1.0682 (6.82)	1.0416 (4.16)	1.0425 (4.25)	0.9612 (3.88)	1.0654 (6.54)
18×35	0.9413 (5.87)	0.9627 (3.73)	0.9599 (4.01)	0.9657 (3.43)	1.0562 (5.62)
21×41	0.9478 (5.22)	0.971 (2.90)	0.9618 (3.82)	0.9708 (2.92)	0.9571 (4.29)
25×49	1.0626 (6.26)	0.9758 (2.42)	0.9631 (3.69)	0.9764 (2.36)	0.9587 (4.13)
29×57	0.9518 (4.82)	1.0225 (2.25)	0.9717 (2.83)	0.9793 (2.07)	0.9648 (3.52)
35×69	1.0487 (4.87)	1.0201 (2.01)	0.9806 (1.94)	1.0185 (1.85)	1.0297 (2.97)

Table 3 Comparison of computed stress intensity factors between collocation method and various types of B-Area method

Nodes	Collocation (Error %)	B-Line (Error %) Type 1	B-Line (Error %) Type 2	B-Line (Error %) Type 3	B-Line (Error %) Type 4
13×25	1.0842 (8.42)	1.0502 (5.02)	1.0581 (5.81)	1.0479 (4.79)	1.0672 (6.72)
15×29	1.0682 (6.82)	0.9562 (4.38)	0.9442 (5.58)	0.9606 (3.94)	1.0651 (6.51)
18×35	0.9413 (5.87)	0.9616 (3.84)	0.9546 (4.54)	0.9639 (3.61)	0.9406 (5.94)
21×41	0.9478 (5.22)	0.9652 (3.48)	0.9588 (4.12)	0.9684 (3.16)	0.9521 (4.79)
25×49	1.0626 (6.26)	1.0301 (3.01)	1.0397 (3.97)	1.0301 (3.01)	1.0413 (4.13)
29×57	0.9518 (4.82)	1.0286 (2.86)	1.0311 (3.11)	0.9784 (2.16)	0.9601 (3.99)
35×69	1.0487 (4.87)	0.9786 (2.14)	0.9768 (2.32)	0.9805 (1.95)	0.9674 (3.26)

conditions.

In the computation, the stress intensity factor is prescribed as $K_I = 1$. Convergence studies are carried out using seven different nodal distributions, with $13 \times 25, 15 \times 29, 18 \times 35, 21 \times 41$, $25 \times 49, 29 \times 57$ and 35×69 nodes. For comparison, the convergence curves for the collocation method and the MELM are plotted in the Fig. 20. By application of the MELM, obtained results are more accurate and stable than those obtained from the collocation method.

Stress intensity factors were computed using the domain form of the J-integral with the domain shown in Fig. 4 (Moran 1978). Tables 2 and 3 list stress intensity factors for different nodal distributions. It can be concluded that the MELM results in more accurate and stable results.

5. Conclusions

The concepts of a newly developed weak formulation, the equilibrium on line method (ELM), were used for construction of a truly meshless method, the meshless equilibrium on line method (MELM). The ELM was previously used by the authors for enforcing the Neumann boundary conditions in the strong-form meshless methods. Based on the concepts of the ELM, weak formulations were proposed and used in the MELM. The resultant method is a novel weak-form meshless method in which all required integrals are simply calculated over straight lines.

Four numerical examples were solved for investigation of the MELM. Obtained results showed that the MLM is more accurate and stable than the collocation method. The superiority of the MELM in stability and accuracy in comparison with the direct collocation method is related to the weak formulation of the MELM.

References

Anderson, T.L. (1991), *Fracture Mechanics: Fundamentals and Applications (1st Edition)*, CRC Press, Boca Raton, FL.

Atluri, S.N. and Zhu, T. (1998), "A new meshless local Petrov-Galerkin (MLPG) approach in computational mechanics", *Comput. Mech.*, **22**, 117-127.

Belytschko, T., Lu, Y.Y. and Gu, L. (1994), "Element-free Galerkin methods", *Int. J. Numer. Meth. Eng.*, **37**, 229-256.

Boroomand, B., Tabatabaei, A.A. and Onate, E. (2005), "Simple modifications for stabilization of the finite point method", *Int. J. Numer. Meth. Eng.*, **63**, 351-379.

Chen, W. and Hon, Y.C. (2003), "Numerical investigation on convergence of boundary knot method in the analysis of homogeneous Helmholtz, modified Helmholtz, and convection-diffusion problems", *Comput. Meth. Appl. Mech. Eng.,* **192**, 1859-1875.

Cleveland, W.S. (1993), *Visualizing Data*, AT&T Bell Laboratories, Murry Hill, NJ.

De, S. and Bathe, K.J. (2000), "The method of finite spheres", *Comput. Mech.*, **25**, 329-349.

Gingold, R.A. and Monaghan, J.J. (1977), "Smoothed particle hydrodynamics: theory and application to non-spherical stars", *Mon. Not. R. Astron. Soc.,* **181**, 375-389.

Golberg, M.A. (1995), "The method of fundamental solutions for Poisson's equation", *Eng. Anal. Bound. Elem.,* **16**, 205-213.

Kansa, E.J. (1990), "Multiquadrics-A scattered data approximation scheme with applications to computational fluid dynamics-II solutions to parabolic, hyperbolic and elliptic partial differential equations", *Comput. Math. Appl.,* **19**, 147-161.

Lancaster, P. and Salkauskas, K. (1981), "Surfaces generated by moving least squares methods", *Math. Comput.*, **37**, 141-158.

Lee, S.H. and Yoon, Y.C. (2004), "Meshfree point collocation method for elasticity and crack problems", *Int. J. Numer. Meth. Eng.,* **61**, 22-48.

Liszka, T.J., Duarte, C.A.M. and Tworzydlo, W.W. (1996), "hp-Meshless cloud method", *Comput. Meth. Appl. Mech. Eng.,* **139**, 263-288.

Liu, G.R. and Gu, Y.T. (2001a), "A point interpolation method for two-dimensional solids", *Int. J. Numer. Meth. Eng.,* **50**, 937-951.

Liu, G.R. and Gu, Y.T. (2001b), "A local point interpolation method for stress analysis of two-dimensional solids", *Struct. Eng. Mech.,* **11**, 221-236.

Liu, G.R. and Gu, Y.T. (2001c), "A local radial point interpolation method (LRPIM) for free vibration analyses of 2-D solids", *J. Sound Vib.,* **246**, 29-46.

Liu, G.R. and Gu, Y.T. (2003), "A meshfree method: meshfree weak-strong (MWS) form method for 2D solids", *Comput. Mech.,* **33**, 2-14.

Liu, G.R., Kee, B.B.T. and Chun, L. (2006a), "A stabilized least-squares radial point collocation method (LS-RPCM) for adaptive analysis", *Comput. Meth. Appl. Mech. Eng.*, **195**, 4843-4861.

Liu, G.R., Li, Y. and Dai, K.Y. (2006b), "A linearly conforming radial point interpolation method for solid mechanics problems", *Int. J. Comput. Meth.,* **3**, 401-428.

Liu, G.R., Dai, K.Y., Han, X. and Li, Y. (2006c), "A mesh-free minimum length method for 2-D problems", *Comput. Mech.*, **38**, 533-550.

Liu, X., Liu, G.R., Tai, K. and Lam, K.Y. (2005), "Radial point interpolation collocation method for the solution of partial differential equations", *Comput. Math. Appl.,* **50**, 1425-1442.

Liu, W.K., Jun, S. and Zhang, Y.F. (1995), "Reproducing kernel particle methods", *Int. J. Numer. Meth. Fl.*, **20**,

1081-1106.
Lucy, L.B. (1977), "A numerical approach to the testing of the fission hypothesis", *Astron. J.*, **82**(12), 1013-1024.
Moran, B. and Shih, C.F. (1978), "Crack tip and associated domain integrals from momentum and energy balance", *Eng. Fract. Mech.,* **27**, 615-641.
Nayroles, B., Touzot, G. and Villon, P. (1992), "Generalizing the finite element method: diffuse approximation and diffuse elements", *Comput. Mech.*, **10**, 307-318.
Onate, E., Idelsohn, S., Zienkiewicz, O.C. and Taylor, R.L. (1996), "A finite point method in computational mechanics: applications to convective transport and fluid flow", *Int. J. Numer. Meth. Eng.,* **139**, 3839-3866.
Perrone, N. and Kao, R. (1975), "A general finite difference method for arbitrary meshes", *Comput. Struct.*, **5**, 45-58.
Sadeghirad, A. and Mahmoudzadeh Kani, I. (2009) "Modified equilibrium on line method for imposition of Neumann boundary conditions in meshless collocation methods", *Commun. Numer. Meth. En.,* **25**, 147-171.
Sadeghirad, A., Mahmoudzadeh Kani, I., Noorzad, A., Rahimian, M. and Vaziri Astaneh, A. (2010), "Elastic fracture analyses using an enriched collocation method", *Arab. J. Sci. Eng.,* **35**, 165-181.
Sadeghirad, A., Mahmoudzadeh Kani, I., Rahimian, M. and Vaziri Astaneh, A. (2009), "A numerical approach based on the meshless collocation method in elastodynamics", *Acta Mech. Sinica.,* **25**, 857-870.
Sadeghirad, A. and Mohammadi, S. (2007), "Equilibrium on line method (ELM) for imposition of Neumann boundary conditions in the finite point method (FPM)", *Int. J. Numer. Meth. Eng.*, **69**, 60-86.
Timoshenko, S.P. and Goodier, J.N. (1970), *Theory of Elasticity, 3rd Edition,* McGraw Hill, New York.
Wang, J.G., Liu, G.R. and Wu, Y.G. (2001), "A point interpolation method for simulating dissipation process of consolidation", *Cornput. Method. Appl. Mech. Eng.,* **190**, 5907-5922.
Zhang, X., Liu, X.H., Song, K.Z. and Lu, M.W. (2001), "Least-squares collocation meshless method", *Int. J. Numer. Meth. Eng.*, **51**(9), 1089-1100.
Zhu, T., Zhang, J.D. and Atluri, S.N. (1998), "Local boundary integral equation (LBIE) method in computational mechanics and a meshless discretization approach", *Comput. Mech.*, **21**(3), 223-235.

Appendix A. The collocation method

The governing Eq. (13) can be rewritten in terms of the displacement field by substituting Eqs. (15)-(17) into Eq. (13).

$$\begin{cases} D_{11}\dfrac{\partial^2 u_x}{\partial x^2}+\dfrac{D_{33}}{2}\dfrac{\partial^2 u_x}{\partial y^2}+\left(\dfrac{D_{33}}{2}+D_{12}\right)\dfrac{\partial^2 u_y}{\partial x\partial y}+b_x=0 \\ \dfrac{D_{33}}{2}\dfrac{\partial^2 u_y}{\partial x^2}+D_{22}\dfrac{\partial^2 u_y}{\partial y^2}+\left(\dfrac{D_{33}}{2}+D_{12}\right)\dfrac{\partial^2 u_x}{\partial x\partial y}+b_y=0 \end{cases} \tag{A.1}$$

The discretized system of equations in a collocation method is formed by substituting the meshless approximation (Eqs. (7), (8)) into governing Eq. (A.1) and collocating the differential equation at each node in the analysis domain. Based on this procedure, discretized equations at inner node $\mathbf{x}_p$ of the problem domain are obtained as

$$\begin{cases} \displaystyle\sum_{i=1}^{n_p}\left(D_{11}\frac{\partial^2\varphi_i}{\partial x^2}+\frac{D_{33}}{2}\frac{\partial^2\varphi_i}{\partial y^2}\right)\hat{u}_{x_i}+\sum_{i=1}^{n_p}\left(\frac{D_{33}}{2}+D_{12}\right)\frac{\partial^2\varphi_i}{\partial x\partial y}\hat{u}_{y_i}+b_x=0 \\ \displaystyle\sum_{i=1}^{n_p}\left(\frac{D_{33}}{2}\frac{\partial^2\varphi_i}{\partial x^2}+D_{22}\frac{\partial^2\varphi_i}{\partial y^2}\right)\hat{u}_{y_i}+\sum_{i=1}^{n_p}\left(\frac{D_{33}}{2}+D_{12}\right)\frac{\partial^2\varphi_i}{\partial x\partial y}\hat{u}_{x_i}+b_y=0 \end{cases}, \quad p=1,2,...,N_r \tag{A.2}$$

where n_p is the number of nodes in the neighborhood of node $\mathbf{x}_p$ for which the weight function $w(\mathbf{x}_p-\mathbf{x}_i)\neq 0$; and N_r is the number of the inner nodes inside the problem domain not belonging to the boundaries.

Dirichlet and Neumann boundary conditions (Eqs. (14a), (14b)) are directly satisfied by substituting the meshless approximation (Eqs. (7), (8)) into Eqs. (14a), (14b). The discretized equations for enforcement the boundary conditions at node $\mathbf{x}_q$ on the Dirichlet boundary and node $\mathbf{x}_s$ on the Neumann boundary are written as

$$\sum_{i=1}^{n_q}\phi_i\hat{u}_i-\bar{u}_q=0, \qquad q=1,\ 2,\ ...,\ N_u \tag{A.3}$$

$$\begin{bmatrix} \displaystyle\sum_{i=1}^{n_s}\left(D_{11}\frac{\partial\phi_i}{\partial x}\hat{u}_{x_i}+D_{12}\frac{\partial^2\phi_i}{\partial y^2}\hat{u}_{y_i}\right) & \displaystyle\sum_{i=1}^{n_s}\frac{D_{33}}{2}\left(\frac{\partial\phi_i}{\partial y}\hat{u}_{x_i}+\frac{\partial\phi_i}{\partial x}\hat{u}_{y_i}\right) \\ \displaystyle\sum_{i=1}^{n_s}\frac{D_{33}}{2}\left(\frac{\partial\phi_i}{\partial y}\hat{u}_{x_i}+\frac{\partial\phi_i}{\partial x}\hat{u}_{y_i}\right) & \displaystyle\sum_{i=1}^{n_s}\left(D_{12}\frac{\partial\phi_i}{\partial x}\hat{u}_{x_i}+D_{22}\frac{\partial^2\phi_i}{\partial y^2}\hat{u}_{y_i}\right) \end{bmatrix} n_i-\bar{t}_s=0, \quad s=1,\ 2,\ ...,\ N_t \tag{A.4}$$

where n_q and n_s are the number of nodes in the neighborhood of node $\mathbf{x}_q$ and $\mathbf{x}_s$ for which the weight function $w(\mathbf{x}_p-\mathbf{x}_i)\neq 0$ and $w(\mathbf{x}_s-\mathbf{x}_i)\neq 0$ respectively; and N_u and N_t are the number of the nodes located on the Dirichlet and Neumann boundaries respectively; $\bar{u}_q$ and $\bar{t}_s$ are the prescribed displacements and tractions over the Dirichlet and Neumann boundaries respectively; and n_i is the unit outward normal vector to the boundary.

Eqs. (A.2), (A.3), (A.4) lead to a system of algebraic equations of the form

$$\mathbf{Ku}=\mathbf{f} \tag{A.5}$$

where $\mathbf{K}$ is the 'stiffness' matrix, $\mathbf{u}$ is the vector of nodal values $\hat{u}_i$ and $\mathbf{f}$ is the 'load' vector. It can be easily seen that the stiffness matrix $\mathbf{K}$ in the presented collocation method is banded because the support domains are compact. However, in general, $\mathbf{K}$ is asymmetric.